



Voltammetric determination of vitamin B₂ by using a highly porous carbon electrode modified with palladium-copper nanoparticles

Arumugam Sangili¹ · Pitchaimani Veerakumar^{2,3} · Shen-Ming Chen¹ · Chellakannu Rajkumar¹ · King-Chuen Lin^{2,3}

Received: 14 December 2018 / Accepted: 29 March 2019 / Published online: 25 April 2019
© Springer-Verlag GmbH Austria, part of Springer Nature 2019

Abstract

Palladium-copper nanoparticles were placed on activated carbon to give a nanocomposite for electrochemical sensing of riboflavin (vitamin B₂). The activated carbon was produced by pyrolysis of natural waste of pistachio nutshells after KOH activation and under a nitrogen atmosphere. The carbons possess a large surface area and micro/meso-porosity. The nanocomposite was characterized by a variety of techniques to confirm structures and morphology. A screen-printed electrode modified with the composite was examined by EIS, CV, DPV, and amperometry. The effects of pH value, scan rate, and stability of the modified electrode were studied. Under optimized conditions, vitamin B₂ displays a well-expressed oxidation peak at -0.15 V (vs. Ag/AgCl) in solutions with a pH value of 7.0. The voltammetric signal increases linearly in the 0.02 to 9 μM concentrations range and a lower detection limit of 7.6 pM. The sensor was successfully applied to the determination of vitamin B₂ even in the presence of other common vitamins and in (spiked) raw milk samples.

Keywords Electrochemical detection · Riboflavin · Cyclic voltammetry · Chronoamperometry · Differential pulse voltammetry

Introduction

A variety of agricultural waste was used to prepare activated carbon (ACs) materials with large surface area, highly porous structure, and many surface functional groups which exhibited attraction for a wide range of applications in electrochemical sensors, energy storage, catalysis, CO₂ capture etc. [1–3]. Many researchers have been devoted to preparing ACs from

agricultural by-products and utilized in multiple disciplines of science like physics, chemistry, and materials science [4, 5]. For instance, sugarcane bagasse [6], fruit shells [7], nutshells [8] etc. have been used as the precursors of ACs. In this work, pistachio nutshell, abundantly available from the pistachio nut processing industries, was utilized as a feedstock for the preparation of ACs, which have been widely used in numerous electrochemical applications [9]. Owing to the unique properties, such as ultra-high surface area, modulated pore size, low toxicity, excellent chemical stability, electrical/thermal conductivity, low cost, and availability of oxygen surface functional groups, nutshells are suitable for preparing AC. They are composed of cellulose, hemicellulose, and other aromatic compounds [10]. Generally, ACs are formed by treating the carbon source with potassium hydroxide (KOH) to afford well-defined pore structures, high specific surface area and topologies [11]. Such ACs with high surface area from an agricultural by-product would be very useful for fabrication of electrode in a suitable voltammetric sensing applications [12].

Carbon supported transition or noble metals, metal oxides and hydroxides, metal alloys, and bimetals, were explored as electrochemical sensors with outstanding performances for high sensitivity, low detection limit, and good stability [13]. Among various transition metals, palladium (Pd) and copper (Cu) nanoparticles were found to be superior in electrocatalytic activity for oxygen reduction reaction [14]. Such Pd-based

Electronic supplementary material The online version of this article (<https://doi.org/10.1007/s00604-019-3396-7>) contains supplementary material, which is available to authorized users.

- ✉ Pitchaimani Veerakumar
spveerakumar@gmail.com
- ✉ Shen-Ming Chen
smchen78@ms15.hinet.net
- ✉ King-Chuen Lin
kclin@ntu.edu.tw

¹ Department of Chemical Engineering and Biotechnology, National Taipei University of Technology, Taipei 10608, Taiwan, Republic of China

² Department of Chemistry, National Taiwan University, Taipei 10617, Taiwan, Republic of China

³ Institute of Atomic and Molecular Sciences, Academia Sinica, Taipei 10617, Taiwan, Republic of China

bimetallic NP systems with changeable structures and morphologies were known to enhance electrocatalytic activity towards the oxidation HCOOH and CH₃OH [15], as well as sensing of H₂O₂ [16]. Yang and his co-workers have demonstrated a three-dimensional nanoporous PdCu alloy-modified GCE in application for the sensing of H₂O₂ and glucose (Glu) [17]. Due to the beneficial synergistic effect between Pd and Cu alloy structure, it exhibited better catalytic activity and durability compared with commercial Pt/C catalysts for CH₃OH oxidation and the ORR. Pd-Cu alloy has greatly enhanced electrocatalytic activity towards HCOOH oxidation. Regarding the electrochemical behaviour of Pd-Cu alloys, the sublayer Cu may provide an electronic modification for the topmost Pd by a surface strain or alloying effects, which produces unique surface sites for HCOOH electro-oxidation [14]. Remarkably, it is well known that the change of *d*-band center of metal catalysts significantly influences their catalytic reaction kinetics by altering the adsorption energies of reaction intermediates. By density functional theory calculation, it has been reported that the insertion of Cu atoms into Pd matrix caused a reduction of the lattice constant and a decrease of the *d*-band centers [15]. Thus, the lower value of *d* band center for Pd-Cu alloy may result in its higher electrocatalytic activity. Moreover, the nanoporous Pd-Cu alloy structure provides good transport channels for electrons and H₂O₂ and Glu molecules to facilitate the reaction kinetics on the Pd-Cu surface [16, 17].

The porous nanostructured composites have attracted increasing attentions in electrochemical sensing of vitamins [18]. Almost all vitamins are organic compounds and need obtained from dietary sources (fruits, vegetable, milk), since they are not produced by the human body. They are essential for the normal functioning of organic metabolism in humans and living animals. Inadequacy of vitamins can lead to different diseases [19]. Vitamins differ in terms of their structure, chemical and biological properties and solubility. The main classification for vitamins is based on solubility, as some are soluble in fat (A, D, E and K) while others are soluble in water (B and C) [20]. Vitamin B₂ or riboflavin (RF; 7, 8-dimethyl-10-riboylisoalloxazine) is a water-soluble vitamin of the B complex, in which the isoalloxazine ring group present in the chemical structure is responsible for the fluorescence and redox properties. And the flavin redox process is thermodynamically reversible, regardless of the number of electrons transferred [21].

A variety of techniques have been utilized in detection such as high performance liquid chromatography (HPLC) [22], spectrophotometry [23], fluorescence detections [24], and microbiological techniques [25]. However, these methods have certain disadvantages such as (i) requiring a time consuming process, (ii) high-cost, and (iii) complicated operating procedures. For the fast and sensitive drug monitoring, electrochemical determination with various modified electrodes were

usually applied for its simplicity, sensitivity, reproducibility and cost efficiency [26].

In this study, the highly porous carbons from pistachio nutshell were synthesized by chemical activation with Pd-Cu alloy NPs deposited on the derived carbon (hereafter denoted as Pd-Cu@NSC) used for the electrochemical sensing of RF in 0.05 M PB solution (pH 7.0). The structural, morphological, and electrochemical properties of the Pd-Cu@NSC nanocomposite modified electrode were successfully characterized. The composite had a unique porous carbon structure, offering more catalytic active sites to allow access of reactants to the catalyst surfaces. The experiment described in this article introduces a green chemical approach for the synthesis of a Pd-Cu@NSC nanocomposite in application for electrochemical sensing of RF. However, the RF detection has some limitation such as selectivity in the presence of interferents and oxygen free working environment. As such, the Pd-Cu@NSC/SPCE exhibited desirable catalytic activity, stability and tolerance towards RF electro-oxidation, indicating the great potential for future applications.

Experimental

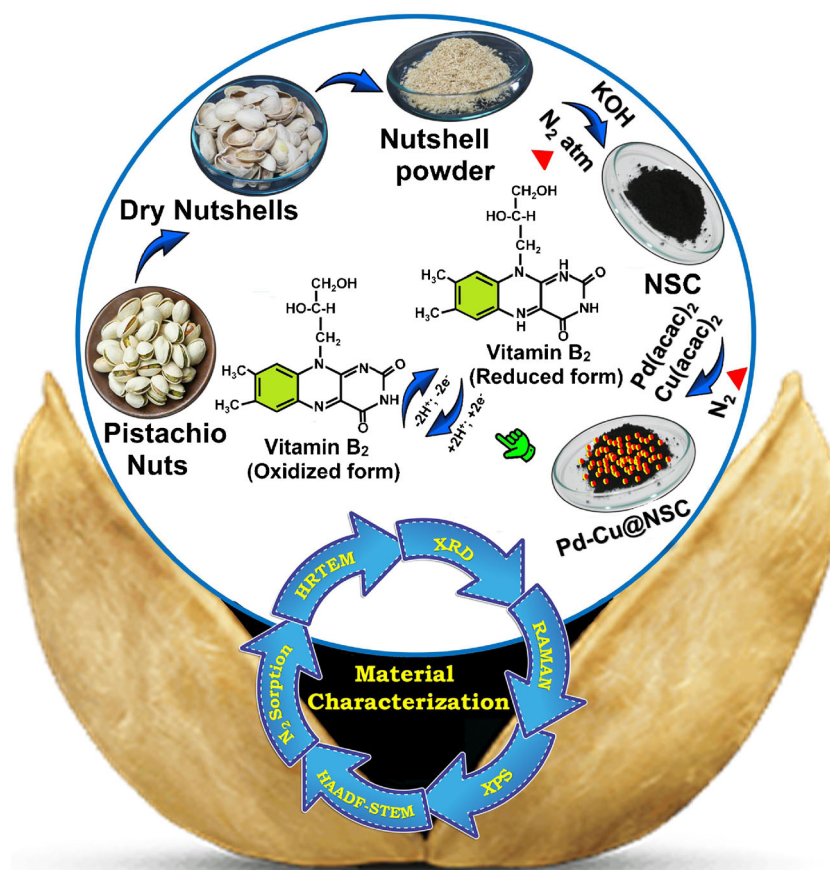
Materials

Palladium(II) acetylacetonate (Pd(acac)₂, 99%), copper(II) acetylacetonate (Cu(acac)₂, metals basis, ≥ 99.9%), riboflavin (C₁₇H₂₀N₄O₆, 98%), potassium hydroxide (KOH, 98%), and potassium ferricyanide (K₃[Fe(CN)₆], 98%) were obtained from Sigma-Aldrich (<http://www.sigmaaldrich.com/taiwan.html>) and used without further purification. Screen printed carbon electrode (SPCE) was purchased from Zensor R&D Co., Ltd. (<http://www.zensor.com.tw/about/about.htm>). The supporting electrolyte used for all the experiments was remained at pH 7.0 phosphate buffer (PB, 0.1 M) solutions prepared by mixing the stock standard solution of Na₂HPO₄ and NaH₂PO₄ of which the pH was adjusted with 0.1 M H₃PO₄ and NaOH. Pistachio nutshells were purchased from the local market and used for carbon preparation (Scheme 1). All other reagents were of analytical grade and used as received and the solutions were prepared by Milli-Q water.

Preparation of the electrode modified with Pd-Cu alloy nanoparticles deposited on nutshell carbon (Pd-Cu@NSC electrode)

At first, Pd-Cu@NSC was prepared as described in ESM. Typically, 1.0 mg of Pd-Cu@NSC composite was dispersed in 1:1 (v/v) of ethanol and water mixture and allowed to sonication for 60 min. The well-dispersed 5.0 μL of Pd-Cu@NSC composite suspension was dropped and casted on the surface of SPCE and dried at room temperature for 3 h. The NSC₇₀₀/

Scheme 1 Schematic diagram of the fabrication of the Pd–Cu alloy nanoparticles deposited on nutshell carbon (Pd-Cu@NSC)s



SPCE, NSC₈₀₀/SPCE, and NSC₉₀₀/SPCE were prepared according to the same conditions for the electrochemical studies.

Choice of materials

Thus far, several efforts have been put forward to fabricate electrode using different carbon nanomaterials (carbon nanotubes, activated carbon, carbon blacks, ordered mesoporous carbons, carbon fibers, carbon aerogels, and graphene). These nanomaterials have been utilized for electroanalytical applications owing to their high electrical conductivity and large surface area. However, they have shown insufficient active sites and time consuming process such that the electrocatalytic applications are limited. Henceforth, biomass is a well-known raw material for the production of carbon materials used in fabrication of electrodes. Since these materials are available in huge quantities and rich in carbon content, such materials can be used to synthesize enriched carbon materials in an environmental friendly way. In the present work, we have fabricated Pd-Cu@NSC composite to be used for riboflavin sensing. It is well-known that the transition metals, specifically Pd, Cu, Ni and Co-doped carbon materials, have good catalytic activity towards various electrocatalysis/sensing applications. However, Pd-Cu has lots of advantages over mono metals such as high stability in neutral pH, lower capacitance current and

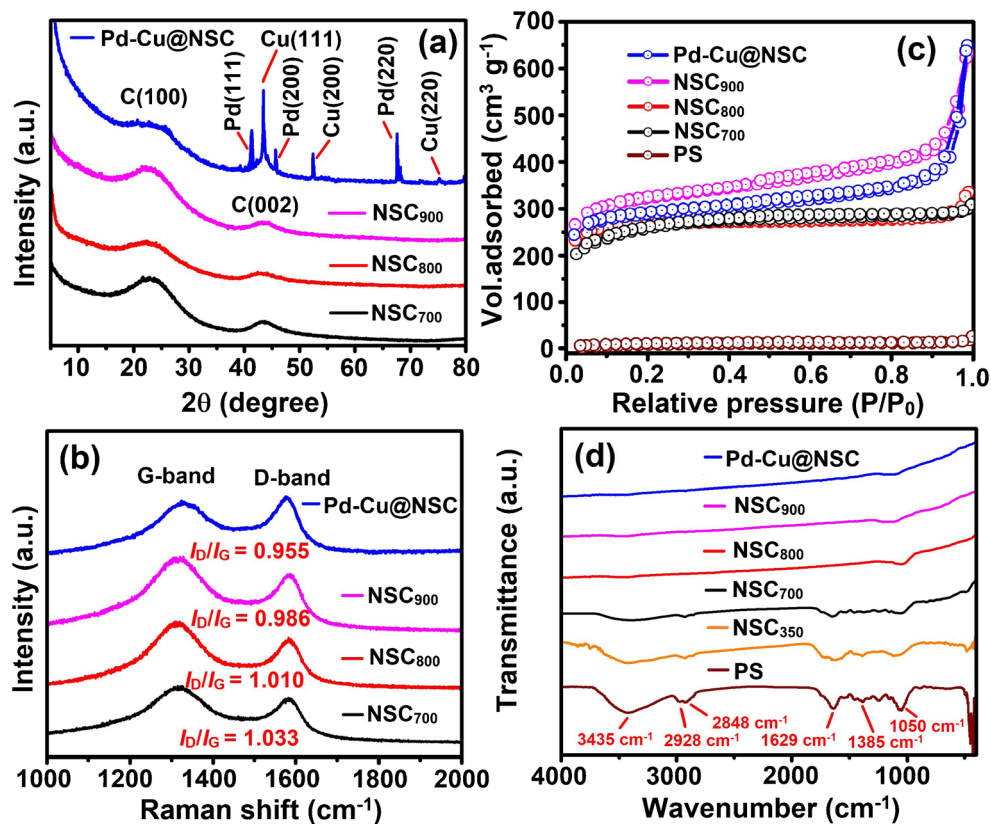
high chemical resistance due to its large surface area and synergistic effect of bimetallic systems. Especially, Pd-Cu@NSC composite may further increase the electrochemically active surface area (or site) of the electrocatalyst. Moreover, this inspires the researcher toward potential utilization of biomass in a more efficient way.

Results and discussion

Characterization of Pd-Cu@NSC nanocomposite

The XRD patterns of the NSCs and Pd-Cu@NSC composite materials are shown in Fig. 1a. All the samples have two broad diffraction peaks at around $2\theta = 24.3^\circ$ and 43.2° in the XRD patterns, which are consistent with the graphitic carbon. The broad diffraction pattern at 2θ of about 24.3° may be attributed to the (002) reflection of the graphitic-type lattice. The weak diffraction pattern at around 43.2° corresponds to a superposition of the (100) and (101) reflections of the graphitic-type lattice, showing only the main characteristic peaks of Pd with a face-centered cubic (*fcc*) structure. The XRD diffraction pattern of Pd-Cu@NSC composite exhibited the characteristic *fcc* crystalline structure of Pd-based materials, of which the peaks located at $2\theta = 41.31, 46.63,$ and 68.66° correspond to

Fig. 1 (a) XRD patterns, (b) Raman spectra, (c) N₂ isotherms, and (d) FT-IR spectra of as-prepared samples



planes (111), (200), and (220), respectively [27]. The Bragg reflections at 43.31, 50.72, and 74.43° can be indexed as the (111), (200) and (220) planes of Cu observed in Pd-Cu@NSC. This indicates that the metallic Pd and Cu have been successfully attached to the surface of the NSC supports.

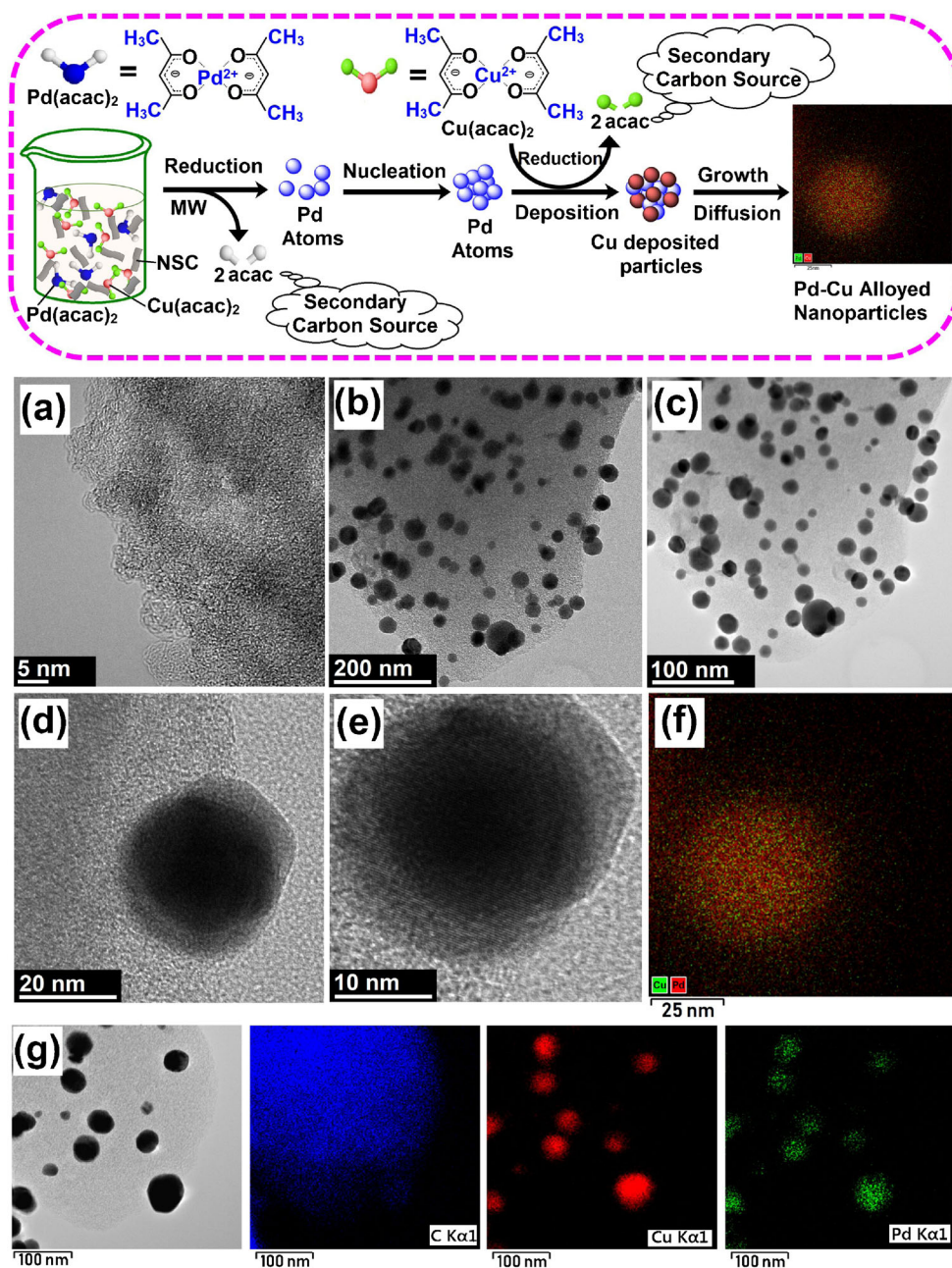
The Raman spectra of the NSCs and Pd-Cu@NSC composite are displayed in Fig. 1b. Two strong peaks at 1347 cm⁻¹ (D band) and 1586 cm⁻¹ (G band) are observed for all carbon materials. The D band refers to the disordered and imperfect structures in the carbonaceous materials, while the G band is related to the vibration of *sp*²-hybridized carbon in the graphite crystallites. The intensity ratio of the D band to G band (I_D/I_G) represents the graphitic degree of the carbons. From the spectra in Fig. 1b, the I_D/I_G ratio of NSC₇₀₀, NSC₈₀₀, NSC₉₀₀, and Pd-Cu@NSC was estimated to be 1.03, 1.01, 0.98, and 0.95, respectively (Table S1). The relatively lower D/G intensity ratio of NSC₉₀₀ indicates a higher degree of graphitization and a decrease in the disordered structure [28]. Notably, compared to the G band at 1586 cm⁻¹ for NSC₉₀₀, the G band of Pd-Cu@NSC (1580 cm⁻¹) showed a downshift due to the incorporation of heteroatoms or metals. In other words, it may be attributed to the supporting alloy Pd-Cu nanoparticle, which decreases the defect sites and the disorder extent in carbon structure [29]. These results are in good agreement with XRD analysis.

Further information on the specific surface area and pore structure of pistachio shell (PS), NSC₇₀₀, NSC₈₀₀, NSC₉₀₀ and

Pd-Cu@NSC (Fig. 2c) is obtained from N₂ sorption isotherm measurements. PS shows a type-II sorption isotherm indicating the non-porous characteristics, while the isotherm profiles of NSCs (NSC₇₀₀, and NSC₈₀₀) obtained by KOH activation completely overlap in the adsorption and desorption of N₂, exhibiting typical type I isotherms, indicative of microporous structures. In this work, KOH played a role as an activation agent for micropore formation during carbonization processing. The porous properties of these materials are summarized in Table S2, including the specific surface area, total pore volume, and average pore diameter. Upon increasing the activation temperatures from 700 to 900, both the surface area and the pore volume increase dramatically from 782.5 m² g⁻¹ and 0.741 cm³ g⁻¹ for the NSC₇₀₀ to 1246.4 m² g⁻¹ and 0.82 cm³ g⁻¹ for NSC₉₀₀, respectively, due to the deepened degree by KOH activation. The average pore diameter increased slightly from 3.1 to 3.8 nm with an increase of the activation temperature from 700 to 900 °C, indicating that larger amount of micro-/mesopores appeared by KOH activation under N₂ conditions [30].

The pore size distribution of various samples were derived from DFT calculations (Fig. S1). Remarkably, both NSC₉₀₀, the Pd-Cu@NSC samples display I/IV-type adsorption/desorption isothermal curves. The S_{BET} surface area of Pd-Cu@NSC (1055.7 cm² g⁻¹) is slightly lower than that of NSC₉₀₀, due to incorporating Pd-Cu NPs onto the NSC₉₀₀ carbon support. Moreover, these mesoporous structure with

Fig. 2 Schematic illustration of the formation mechanism of Pd-Cu alloy NPs (Top), FE-TEM images of (a) pristine NSC, (b, c) Pd-Cu@NSC composite, (d, e) FE-TEM image of an individual Pd-Cu alloy nanoparticle on NSC, (f) HAADF-STEM image of Pd (green dots) and Cu (red dots) elements in Pd-Cu@NSC, and (g) the corresponding elemental mapping images (bottom)



large micro and mesopores provide a large number of active sites to facilitate the electron transfer or analyte diffusion/ions transportation, and therefore can potentially enhance the sensing performance when used as electrode [31].

Figure 1d shows the FT-IR spectra of PS, NSC₃₅₀, NSC₇₀₀, NSC₈₀₀, NSC₉₀₀, and Pd-Cu@NSC samples from 400 to 4000 cm^{-1} . It was noticed that some of the peaks available in pistachio shell (PS) appeared around 3435 cm^{-1} which was mainly attributed to chemisorbed water molecules and hydroxyl groups of O-H stretching mode. On the other hand, the peaks appearing at around 2928, 2848 and 1385 cm^{-1} were caused by methylene asymmetric C-H stretching, methylene symmetric C-H stretching and

methyl symmetrical C-H bending, respectively [32]. In addition, the C=C stretching around 1629 cm^{-1} is assigned to the characteristic vibrations in aromatic rings, whereas the sharp peak at 1050 cm^{-1} in PS is due to C-O stretching. Compared to raw materials (PS), the number of vibrational modes are largely diminished due to the reduction of functional groups in the PS, indicating that carbonization, especially at higher temperatures from 700 to 900 $^{\circ}\text{C}$, increases the aromatic carbon content but decreases aliphaticity. A similar observation was previously reported for the PS at different carbonization conditions. However, at temperatures higher than 350 $^{\circ}\text{C}$, the decreased intensity of related peaks is indicative of the transformation of the native carbon

structure to polycyclic aromatic structures during carbonization, as displayed in Fig. 1d.

The KOH activated carbons obtained at 700, 800 and 900 °C have been observed by SEM, and the micrographs were given in Fig. S2. The metal precursors such as Pd(acac)₂ and Cu(acac)₂ are suitable metal organic compounds for the synthesis of Pd and Cu NPs. In the present work, we focused on the development of Pd-Cu alloy phases by microwave (MW)-thermal reduction of Pd and Cu salts. To obtain Pd-Cu alloy NPs, the decomposition temperature (*t*_{dec}) of Pd(acac)₂ at 160 °C, and Cu(acac)₂ at 286 °C should be taken into account. At first, the Pd precursor is reduced within seconds and nucleates to form seeds with low crystallinity, i.e., a small amount of Pd atoms aggregate to Pd NP seeds at nucleation stage. Next, the subsequent supply and reduction of Cu precursor enables the deposition of reduced atoms on the Pd particle surface [33]. Then, the low supersaturation suppresses further homogeneous nucleation. Surface atoms then diffuse into the particle to form an alloyed nanoparticle with the assistance of the high temperature (MW)-thermal reducing method. Now, the growth proceeds to deposit more Pd-Cu species around the nuclei, forming the Pd-Cu alloy NPs. The schematic representation of the formation of Pd-Cu alloy nanostructure process is reported in Fig. 2 (top).

To support the above mechanism, the representative FE-TEM images of the Pd NPs, Cu NPs, and Cu-Pd alloy NPs supported NSC are shown in Fig. S3a-f, respectively. All of the Cu-Pd alloy NPs in the TEM images (Fig. S3d-f) show that the distribution of the alloy metal nanoparticles is very homogeneous with an average diameter of ca. 35.6 nm. In addition, the FE-SEM micrographs of the Pd-Cu NPs grafted on the surface of porous NSC can be observed (Fig. S4a,b). Under microwave irradiation, the metal salts are effectively decomposed and completely reduced to zero state. After the nucleation, Pd-Cu NPs are uniformly anchored on the NSC matrix with average diameters of ca. 60–75 nm.

A typical EDS spectrum of Pd-Cu@NSC confirms existence of the C, O, Cu and Pd elements (Fig. S3d); the sample is mainly composed of C (73.66 atom%), O (12.78%), Pd (7.45%), and Cu (6.11%) elements (see inset, Fig. S4c). The presence of absorption peaks at ca. 2.8 and 0.9 keV due to surface plasmon resonance confirms the formation of Pd-Cu alloy structure [33]. For this sample, the atomic ratio of Pd to Cu in Pd-Cu NPs is ca. 1:1.21 on the porous carbon surfaces.

The FE-TEM of NSC and Pd-Cu@NSC samples are shown in Fig. 2. The FE-TEM image of pristine NSC exhibits highly mesoporous structures (Fig. 2a). From the morphology observation (Fig. 2a), it can be concluded that KOH activation treatment had a significant impact on the porous structure and morphology of the resulting NSC. The homogeneous distributions of the fcc morphological Pd-Cu NPs on the NSC surface indicate that no nanoparticles were segregated (Fig. 2b,c). The diameters of most binary Pd-Cu NPs were in the

range of 10–30 nm. The carbonaceous materials may be controlled the morphologies of the formation of a binary Pd-Cu NPs with the fcc structure during the reaction, which had a crucial role during nucleation and stabilization using MW irradiation. The high-resolution FE-TEM images of the Pd-Cu@NSC composite in Fig. 2d,e revealed that the alloy Pd-Cu NPs encapsulated in the NSC substrate typically have an average size of ~30 nm. The lattice fringes with a spacing of ca. 0.215–0.218 nm are observed in the magnified FE-TEM image (Fig. S5a). The SAED pattern displays the continuous diffraction rings (Fig. S5b), indicating the Pd-Cu@NSC composite are polycrystalline [34].

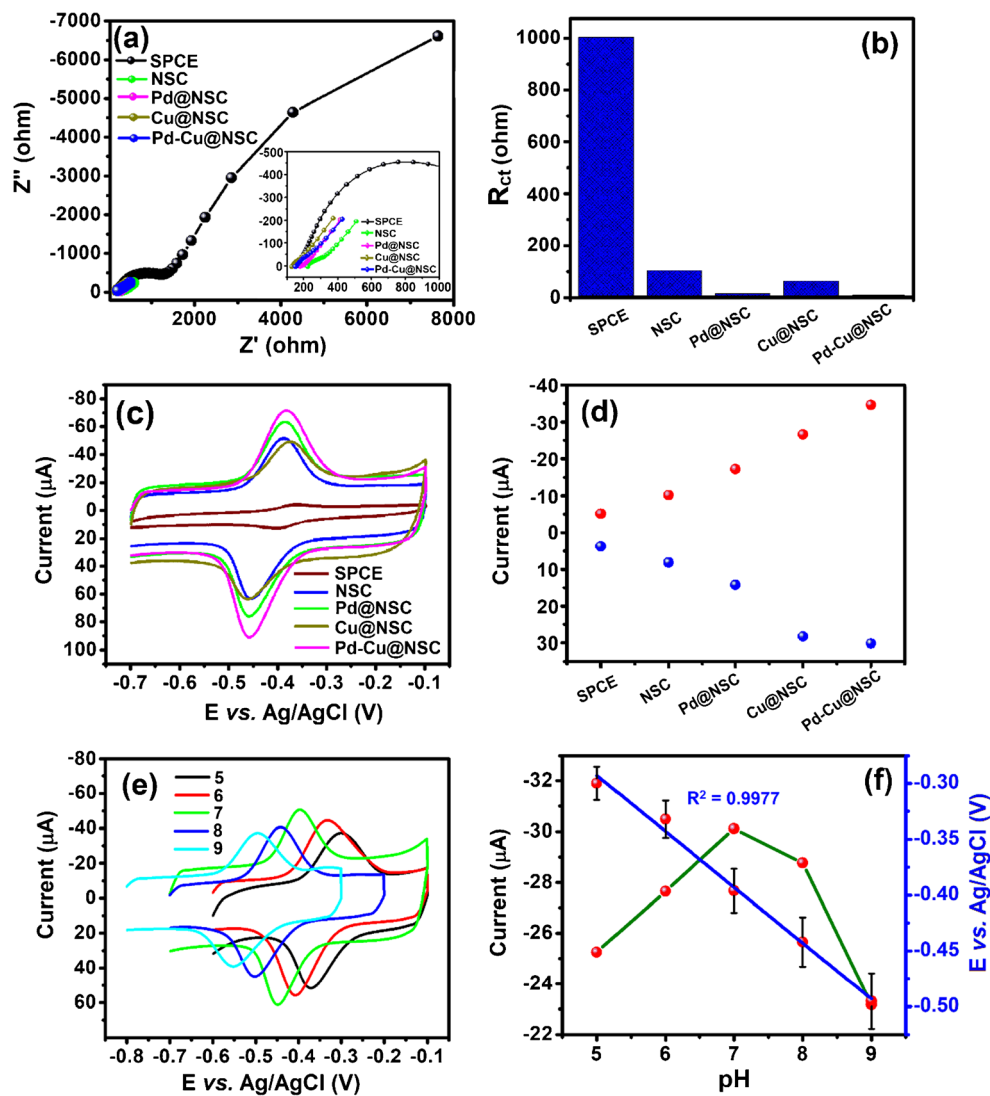
The HAADF-STEM image (Fig. 2f) and elemental mapping of an individual Pd-Cu@NSC revealed that each Pd and Cu element was uniformly distributed on the NSC support (Fig. 2g). The mapping images of C (blue dots) from carbon support, Pd (green dots) and Cu (red dots) elements clearly indicate an inhomogeneous distribution of binary Pd-Cu alloy NPs; the large amount of the Pd atoms appeared to reside on the Cu crystalline particles (Fig. 2f). All these results evidenced that bimetallic Pd-Cu alloy NPs were successfully embedded onto the NSC support.

XPS is a kind of surface sensitive technique to analyze the chemical composition of Pd-Cu@NSC composite. The survey scan (Fig. S6a) shows the surface elements are C, O, Pd, and Cu. The C 1s spectra of Pd-Cu@NSC sample is deconvoluted into four components: the peaks at 282.8 eV (C₁), 283.5 eV (C₂), and 284.3 eV (C₃), are attributed to C-C, C=C, and C-O of the graphitic structures, respectively. The last peak at 290.1 eV (C₄) is assigned to the π-π* shake-up satellite bonding, as shown in Fig. S6b [27]. From Fig. S6c, it can be seen that the broader O 1s peak of the Pd-Cu@NSC sample can be fitted with three components. The peaks at 531.2 eV (O₁), 531.8 eV (O₂), and 532.4 eV (O₃) were attributed to the C-O, C=C, and C-O-C/C-OH groups, respectively. In addition, the Pd 3d signal of the Pd-Cu@NSC composite (Fig. S6d) was fitted into two pairs of doublets with a BE of ca. 336.4 (Pd 3d_{3/2}), 338.8 eV (3d_{5/2}), 342.1 (Pd 3d_{3/2}) and 343.6 eV (3d_{5/2}), which can be ascribed to Pd⁰ and Pd^(II) species, with a ratio (1:0.13) which is much closer to the other report [16]. Moreover, the characteristic peaks from Cu are clearly observed at 935.3 eV and 952.2 eV, indicating the Cu 2p_{3/2} and Cu 2p_{1/2} core-levels (Fig. S6e), similar to the result of Pd-Cu alloy NPs [16]. The results have provided new insights into the structure-composition, which is important for the design of nanoalloy catalysts with tunable catalytic properties.

Electrochemical studies

Electrochemical impedance spectra (EIS) measurements of [Fe(CN)₆]^{3-/4-} system were performed to investigate the electron transfer resistance (*R*_{ct}) and conductivity of different electrodes as shown in Fig. 3a. From these plots the charge

Fig. 3 (a) Measured Nyquist plots, (b) Fitted R_{ct} values, (c) CV profiles of the bare SPCE, the pristine NSC-, Pd@NSC-, Cu@NSC-, and Pd-Cu@NSC/SPCE, and (d) the corresponding peak current responses for electro-oxidation of RF over various modified electrodes, (e) Pd-Cu@NSC/SPCE at different electrolyte pH, and (f) various pH vs variations of oxidation peak potential and redox peak current



transfer resistance (R_{ct}) of the bare SPCE, NSC, Pd@NSC, Cu@NSC, and Pd-Cu@NSC composite are calculated to be 996, 98.2, 11.64, 58.52, and 4.88 Ω , respectively. All the fitted R_{ct} values are summarized in Fig. 3b for comparison. Notice that the fabricated electrode based on Pd-Cu@NSC exhibits a much smaller R_{ct} value than those of bare SPCE, NSC-, Pd@NSC-, Cu@NSC/SPCE, and indicating that Pd-Cu@NSC/SPCE provides excellent conductivity and electron transfer resistance to allow for occurrence of a faster charge transfer process. The Nyquist plots of bare SPCE, NSC₇₀₀, NSC₈₀₀, and NSC₉₀₀ measured in 1.0 mM $[\text{Fe}(\text{CN})_6]^{3-/4-}$ in 0.1 M KCl electrolyte are given in Fig. S7a and Fig. S7b. The obtained results show that the NSC₉₀₀ with a smaller R_{ct} value owns superior electron transfer properties.

The electrocatalytic activity of Pd-Cu@NSC composite was investigated by performing cyclic voltammetry (CV) to detect RF. The CV response for bare SPCE, pristine NSC, Pd@NSC, Cu@NSC, and Pd-Cu@NSC/SPCE in N_2 -saturated 0.05 M PB solution (pH 7.0) containing 50 μM RF at

50 mV s^{-1} (-0.7 to -0.1 V (vs. Ag/AgCl)) are shown in Fig. 3c. The plot of corresponding peak current vs various modified electrodes is given in Fig. 3d. In addition, the CV was performed on the effect of different calcination of Pd-Cu doped NSC/SPCE towards RF sensing, and the resulting plots for the redox peak current with different modified Pd-Cu doped NSCs/SPCE are given in Fig. S7c and Fig. S7d. The Pd-Cu@NSC/SPCE was demonstrated to have higher redox peak current. Therefore, NSC₉₀₀ supported Pd-Cu modified electrode was selected for further electrocatalytic sensing of RF. The relationship between peak current and bare NSCs is also plotted in Fig. S7c and Fig. S7d. Notice that the NSC exhibits a weak redox peak due to the restriction of both electrons transfer and mass transport. In contrast, Pd-Cu@NSC shows a well characteristic redox peak, evidencing that the doping Pd-Cu metal may facilitate electron transfer on the surface of the NSC matrix. Further, the redox peak currents are intensively increased at modified SPCE, because of the presence of a large number of metal active sites (Pd-Cu) to

enhance their catalytic behaviour and porous nature of carbon to improve the electron transfer process. As a result, the synergistic effects of Pd-Cu alloy NPs and NSC boosted the electrocatalytic activities and rapid electron transfer process towards electro-oxidation of RF.

The effect of pH on Pd-Cu@NSC/SPCE was examined in the presence of 50 μM RF at a scan rate 50 mV s^{-1} by CV, as displayed in Fig. 3c. It shows that both oxidation and reduction peak for RF were well defined at each pH value. When the pH increased from 5 to 7, the redox peak current of RF gradually increased. Then, the redox peak current decreased in RF with further increasing pH from 7 to 9. In addition, the redox peak potential shifted to more negative direction upon increasing the pH 5 to 9. Interestingly, the highest redox peak current response was observed at pH 7.0 (Fig. 3e green line). In Fig. 3f blue line shows the linear relationship between pH in the range of 5 to 9 and the formal potential $[(E_{pa} + E_{pc})/2]$, as expressed by $I_p = 0.04795\text{pH} - 0.08885$ with $R^2 = 0.9977$. The obtained slope of 47.9 mV/pH is very close to the theoretical value (59 mV).

Furthermore, the electro-oxidation of RF was found to involve equal number of protons (2H^+) and electrons (2e^-) transfer reaction on the modified electrode surface. The voltammetric electrocatalysis of RF takes place at flavin group of RF which is capable of undergoing redox reactions. The probable reaction mechanism is presented in Scheme 2.

It is noticed that Cu as an assistant component plays important roles in enhancing the catalytic activity of Pd. [14–17] Electronic properties would be changed due to the d-band center shifts during the formation of Pd-Cu alloy, and the synergistic effect of the composition further increases the electrochemical sensing towards biomolecules. Moreover, this bimetallic alloy of Pd with Cu not only exhibits higher catalytic activity for RF sensing, but also reduces the cost of the catalyst significantly.

As shown in Fig. 4a, the electrocatalytic response by CV was acquired in the presence of different concentration of RF from 25 to 100 μM in 0.05 M PB solution (pH 7.0) at a scan rate of 50 mV s^{-1} . The redox peak current of RF was found to increase linearly with increasing the concentrations of RF from 25 to 100 μM . Figure 4b shows the

linear calibration plot of the concentration of RF versus redox peak current, following the linear regression equation of $I_{pa} = 1.0097x - 14.531$ ($R^2 = 0.9996$) and $I_{pc} = 0.843x + 9.848$ ($R^2 = 0.9982$). The results indicate the excellent electrocatalytic behavior of Pd-Cu@NSC/SPCE towards the detection of RF.

To examine the reaction kinetics, the CV profiles of RF with Pd-Cu@NSC/SPCE were scanned by changing the rates from 10 to 100 mV s^{-1} in a 50 μM RF 0.05 M PB solution (pH=7), as shown in Fig. 4c. The CV results show that the redox peak current increased with increasing the scan rate (ν) in the range from 10 to 100 mV s^{-1} . Figure 4d shows the linear calibration plot between scan rate and redox peak current of RF, following a linear regression equation of $I_{pc} (\mu\text{A}) = 1.0333x - 1.1248$ ($R^2 = 0.9989$) and $I_{pa} = 0.893\nu (\text{mV s}^{-1}) - 0.9735$ ($R^2 = 0.9969$). Notably, the above result suggests that the reaction kinetics should be controlled by adsorption and reversible process. The electrochemical parameters such as electron transfer co-efficient (k_s) and charge transfer co-efficient (α), which can be calculated using Laviron's model [35]. According to this model the following equation is expressed: (1–3)

$$E_{pa} = E^{0'} + \left(\frac{2.3RT}{(1-\alpha)nF} \right) \ln \nu \quad (1)$$

$$E_{pc} = E^{0'} - \left(\frac{2.3RT}{\alpha nF} \right) \ln \nu \quad (2)$$

$$\log k_s = \alpha \log(1-\alpha) + (1-\alpha) \log \alpha - \log \left(\frac{RT}{nF\nu} \right) - (1-\alpha) \frac{\alpha nF \Delta E}{2.3 RT} \quad (3)$$

where n is the number of electron transferred, $R = 8.314 \text{ J K}^{-1} \text{ mol}^{-1}$ is the gas constant, $T = 25 \text{ }^\circ\text{C}$ is the temperature, F is the Faraday's constant ($96,485 \text{ C mol}^{-1}$) and others are in their usual meanings. Generally, α is assumed to be 0.5 in a fully irreversible electrode process [35], and thus the electron transfer number is evaluated to be 2. As demonstrated above, the electro-oxidation of RF at Pd-Cu@NSC/SPCE involves a two-proton and two-electron process (see Scheme 2).

Furthermore, DPV technique was applied to measure the analytical performance of the Pd-Cu@NSC/SPCE toward the determination of RF. Figure 5a shows the DPV analysis of the

Scheme 2 Electro-oxidation mechanism of RF on Pd-Cu@NSC/SPCE

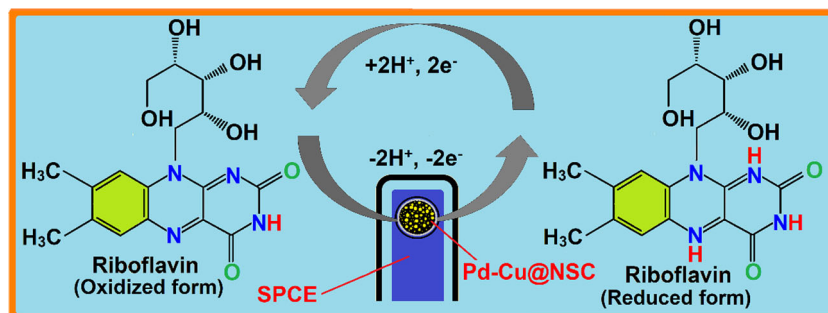
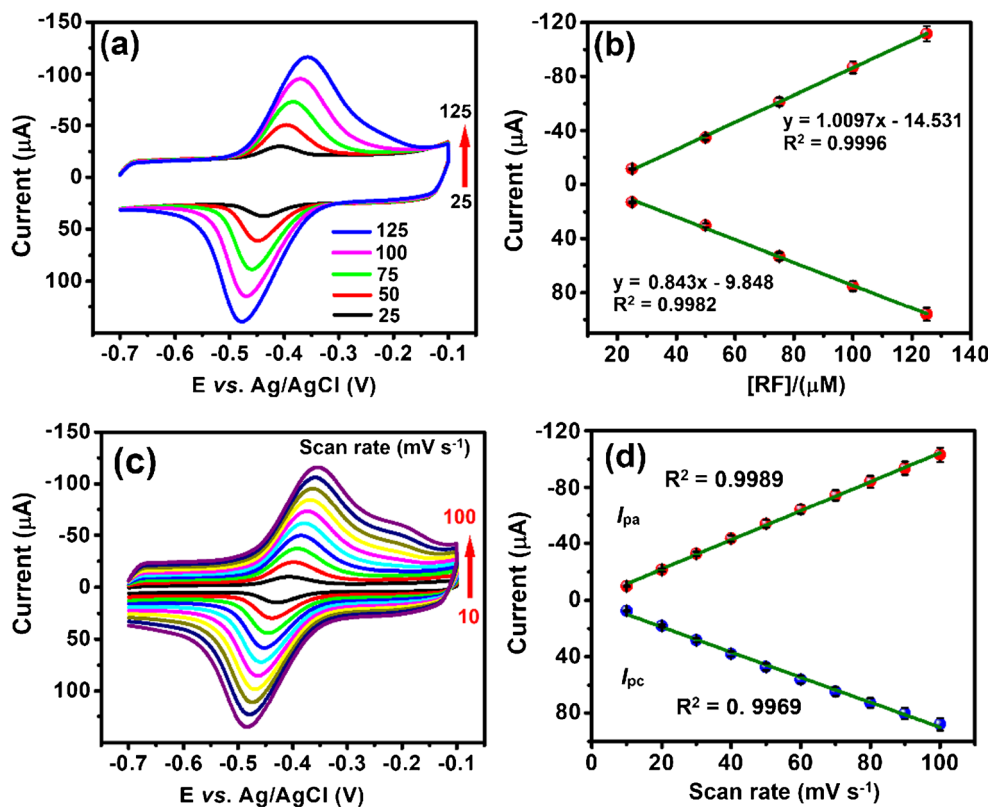


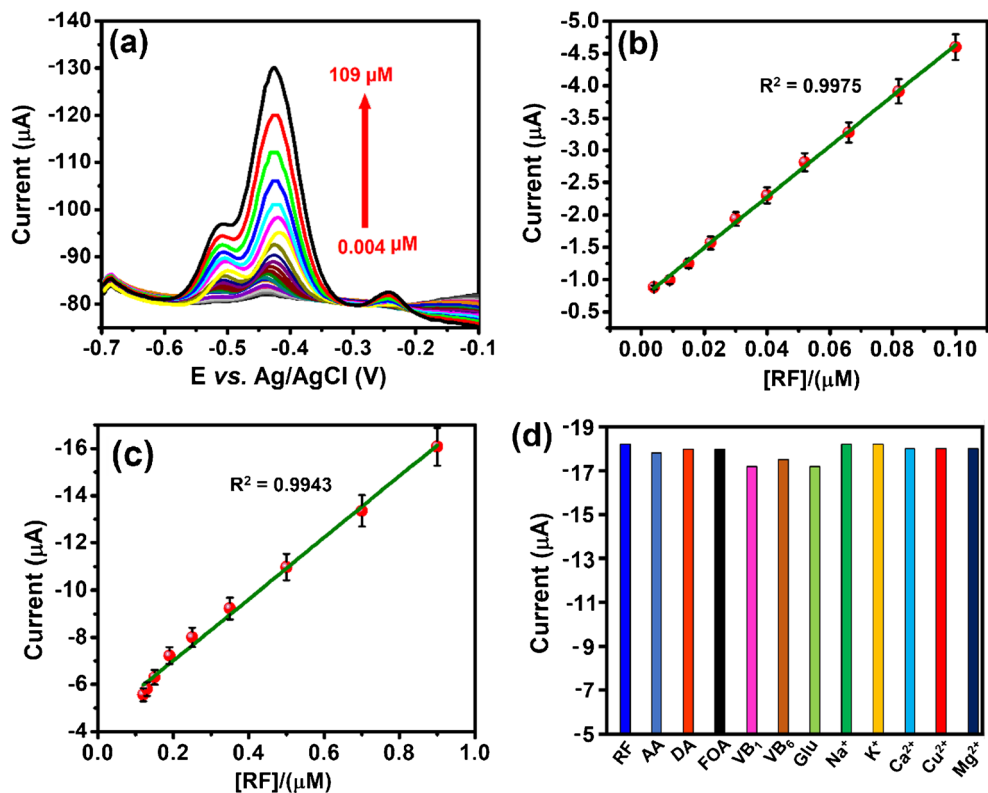
Fig. 4 (a) CV profile of different concentration of RF (25–125 μM) and (b) corresponding correlation plot of peak oxidation current vs concentration of RF over the Pd-Cu@NSC/SPCE. (c) CV profile, and (d) corresponding correlation plot of peak oxidation current vs scan rate in N_2 -saturated PB solution (pH = 7.0) containing 50 μM RF recorded at different scan rates from 10 to 100 mV s^{-1} (-0.7 to -0.1 V (vs. Ag/AgCl))



electrochemical oxidization of RF in pH 7.0 solution under optimized working conditions. As can be clearly seen, the electrocatalytic oxidation of RF is gradually increased with

increasing the RF concentration from 0.004–109 μM . Two linear ranges between the oxidation peak current and concentration of RF were observed. The first linear proportion of the

Fig. 5 DPV curves for the Pd-Cu@NSC/SPCE in the presence of (a) varied [RF] in the range of 0.04–109 μM , (b, c) their corresponding calibration plots for peak current vs. RF concentration, and (d) Variations of peak oxidation current in the presence of RF and co-existence of different interferences (AA, DA, FOA, VB₁, VB₆, Glu, Na⁺, K⁺, Cu²⁺, and Mg²⁺)



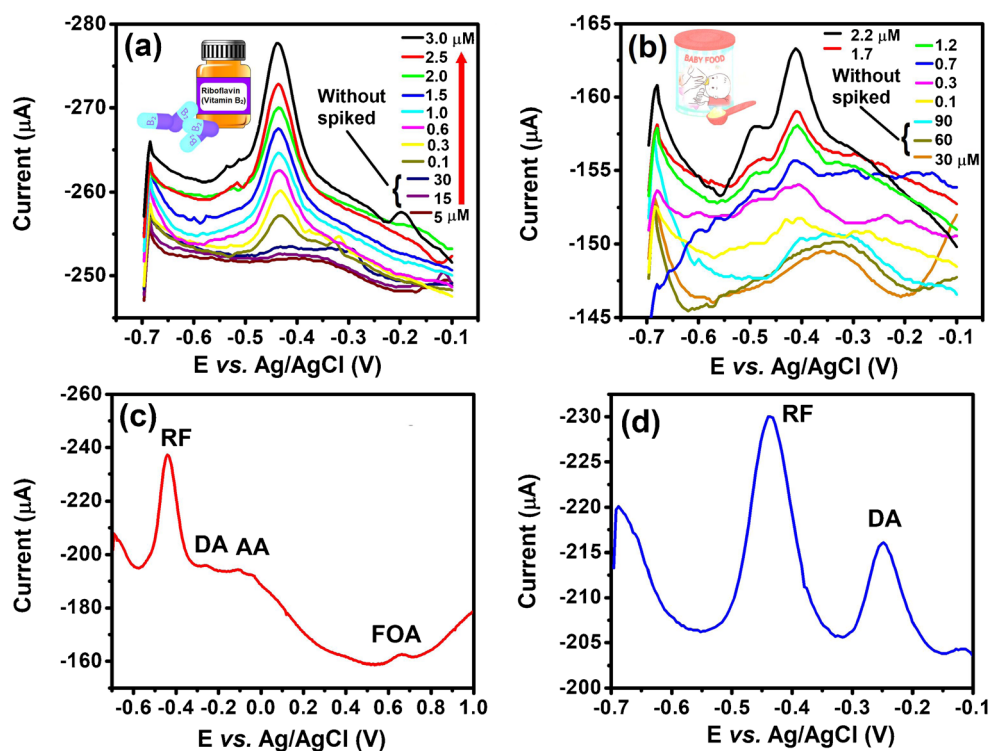
RF concentration range (Fig. 5b) was expressed by I_{pa} (μA) = $39.2165C$ (μM) - 0.7092 with a correlation co-efficient $R^2 = 0.9975$, while the second linear range was from 0.004 – 0.1 μM , following a linear regression equation: I_{pa} (μA) = $13.031C$ [μM] - 4.4055 with a correlation coefficient (R^2) of 0.9943 (Fig. 5c). Notably, higher sensitivity and very lower limit of detection (LOD) of 163.4 μA μM^{-1} and 7.64 pM ($3\sigma/b$) were calculated by using the slope of the first linear response (low level: 0.004 – 0.1 μM), where σ is the standard deviation of the blank signal based on measurements on the blank solution, and b is the slope of the calibration plot.

Mehmeti et al. [18] also reported the RF detection by using manganese dioxide-modified carbon paste electrode (MnO_2/CPE). They achieved dynamic linear range of 0.02 – 9 μM , 15 nM LOD, good reproducibility ($\pm 3\%$) and repeatability ($\pm 2\%$). Some possible interfering compounds such as vitamin (VB_1), vitamin B_6 (VB_6), vitamin B_{12} (VB_{12}), ascorbic acid (AA) and Glu, were also tested. Moreover, this method was successfully applied to the determination of RF in pharmaceutical samples with range of 95 – 97% recovery. Parvin team fabricated a sensitive and selective electrochemical probe of ferromagnetic nanoparticle-incorporated triazine dendrimer (FMNPs@TD) on a modified gold (Au) electrode (Au/PPy/FMNPs@TD) [20]. They also studied an efficient voltammetric sensing of water soluble $\text{V}_{\text{B}_{12}}$ with a wide linear range (4.0 – 500.0 nM), and LOD (0.62 nM) with a R^2 of 0.9967 . This result suggests that the modified electrode is quick, relatively economic,

reliable, and suitable for the detection of $\text{V}_{\text{B}_{12}}$. As can be seen from Fig. 5d, no significant change was observed during detection of RF even in the co-presence of excess amount of interferents, such as AA, dopamine (DA), folic acid (FOA), vitamin B_1 (VB_1), vitamin B_6 (VB_6), (Glu), Na^+ , K^+ , Ca^{2+} , Cu^{2+} , and Mg^{2+} , thereby making the SPCE as robust and selective RF detection even for real sample analysis. Apart from some anions, cations, and organic compounds that may exist in real food samples were selected. The results are displayed in Fig. S9. The results show that the adding of some organic substances such as uric acid, purine, pyrimidine, isalloxazine, adinine, guanine, kaempferol, myricetin, apigenin, and quercetin do not interfere the determination of RF. In addition, we have also performed quantitative analysis of RF using the traditional HPLC method toward the sensing of RF in various real samples and the recovery data are summarized in Table S5. The results reveal that the SPCE can be exploited for detection of RF. Additionally, the analytical parameters such as linear range and LOD were comparable to the previously reported RF sensors as shown in Table S3.

For practical application, the Pd-Cu@NSC/SPCE was used to detect commercially available riboflavin tablets and milk powder samples. Riboflavin and B complex tablets were purchased from the local drug store and milk powder (Nestle Foods, Taiwan) was purchased from the local supermarket, which were taken for the RF real sample analysis. The tablets were weighed, and then made

Fig. 6 DPV curves obtained from the Pd-Cu@NSC/SPCE in the presence of varied loading of (a) RF vitamin tablets (without spiked $5, 15, 30$ and with spiked $0.1, 0.3, 0.6, 1.0, 1.5, 2.0, 2.5$ and 3.0 μM), (b) milk samples (without spiked $30, 60, 90$ μM with spiked $0.1, 0.3, 0.7, 1.2, 1.7, 2.2$ μM) in PB (pH 7.0), (c) DPV recorded of simultaneous electro-oxidation of RF over RF (3.0 μM), DA (10 μM), AA (200 μM), and FOA (50 μM) molecules, and (d) A separate DPV recorded of simultaneous electro-oxidation of RF over DA



into a fine powder with a mortar. Then, it was mixed with 50 mL of deionized water, sonicated for 30 min, and then filtered using Whatman 1 (55 mm diameter) filter paper followed by centrifugation at 6000 rpm. The resulting supernatant solutions were further used for real sample analysis. Then, the solution was diluted twice using PBS (pH 7.0) and the DPV was carried out using the standard addition method.

For milk samples, typically a weighed amount of milk powder was dissolved in boiling water and the proteins were precipitated out by the addition of glacial acetic acid and digested for 15 min in a water bath. The solution was filtered using Whatman 1 (55 mm diameter) filter paper followed by centrifugation at 6000 rpm. The pH of the diluted filtrate was adjusted with boric and orthophosphoric acid to pH 7. The sample analysis was carried out by DPV technique using a recovery test method, as depicted in Fig. 6a, b. From Table S4, the recovery of RF was in the range of 95.08–100.8%, indicating that the SPCE can be successfully applied for the detection of RF in real sample analysis.

The storage stability experiment was conducted by CV with 25 μM of RF for 20 days under the same experimental conditions of Pd-Cu@NSC/SPCE. The results show loss only 8.5% of the redox peak current response from the initial peak current value. In addition, the reproducibility of five different SPCEs was tested and their current response towards the oxidation of 25 μM of RF in PB solution (0.05 M, pH 7.0) yielded a RSD value 2.8%. The redox peak response current, revealing a satisfactory stability for the detection of RF, indicates that our device can offer superior reproducibility as a RF sensor. DPV response of RF was acquired in the presence of equal concentration of potential interference VB₆, and VB₁₂, and 50 times higher concentration of Glu, Mg²⁺, Ca²⁺ and Cu²⁺ ions. The results show only less than $\pm 5\%$ current changes. Figure 6c shows the simultaneous determination DPV response of RF (3.0 μM), DA (10 μM), AA (200 μM), and FOA (50 μM) electroactive molecules. Additionally, we checked the simultaneous determination of potential interfering compound of 3.0 μM of RF with DA in a separate experiment (Fig. 6d). Clearly, the RF peak appeared at different position from the interferents.

Conclusions

In summary, a Pd-Cu@NSC/SPCE based electrochemical sensing of RF was successfully demonstrated for the first time. The Pd-Cu@NSC/SPCE has excellent electro-oxidation performance towards RF sensing due to large surface area, surface functionality, good conductivity, and fast electron transfers. Hence, this work demonstrated a good linear range in the concentration (0.004–0.1 μM) yielding a LOD of 7.64 pM, with a good current sensitivity of 163.4 $\mu\text{A } \mu\text{M}^{-1} \text{ cm}^{-2}$. In

addition, the SPCE achieved an excellent reproducibility, stability, selectivity for detection of RF, and applicable to sensing in various real samples with satisfactory recoveries, thereby showing better performance than other electrodes of study.

Acknowledgments The authors are grateful for the financial support (MOST 106- 2113-M-027-003-MY3 to S.-M.C. and MOST-102-2113-M- 002-009-MY3 to K.-C.L.) from the Ministry of Science and Technology (MOST), Taiwan.

Compliance with ethical standards The author(s) declare that they have no competing interests.

References

- Hassan M, Zhang S, Lind J, Wang T, Bo X, Lin H, Li WH, Zhou M (2018) The biomass of ground cherry husks derived carbon nanoplates for electrochemical sensing. *Sensors Actuators B Chem* 255(3):3248–3256. <https://doi.org/10.1016/j.snb.2017.09.151>
- Lam E, Luong JHT (2014) Carbon materials as catalyst supports and catalysts in the transformation of biomass to fuels and chemicals. *ACS Catal* 4(10):3393–3410. <https://doi.org/10.1021/cs5008393>
- Veerakumar P, Rajkumar C, Chen SM, Thirumalraj B, Lin KC (2018) Activated porous carbon supported rhenium composites as electrode materials for electrocatalytic and supercapacitor applications. *Electrochim Acta* 271(1):433–447. <https://doi.org/10.1016/j.electacta.2018.03.165>
- Iřitan S, Ceylan S, Topcu Y, Hintz C, Tefft J, Chellappa T, Guo J, Goldfarb JL (2016) Product quality optimization in an integrated biorefinery: conversion of pistachio nutshell biomass to biofuels and activated biochars via pyrolysis. *Energy Convers Manag* 127(1):576–588. <https://doi.org/10.1016/j.enconman.2016.09.031>
- Veerakumar P, Maiyalagan T, Raj BGS, Guruprasad K, Jiang Z, Lin KC (2018) Paper flower-derived porous carbons with high-capacitance by chemical and physical activation for sustainable applications. *Arab J Chem*. <https://doi.org/10.1016/j.arabjch.2018.08.009>
- Rufford T, Hulicova-Jurcakova D, Khosla K, Zhu Z, Lu GQ (2010) Microstructure and electrochemical double-layer capacitance of carbon electrodes prepared by zinc chloride activation of sugar cane bagasse. *J Power Sources* 195(3):912–918. <https://doi.org/10.1016/j.jpowsour.2009.08.048>
- Lou BS, Veerakumar P, Chen SM, Veeramani V, Madhu R, Liu SB (2016) Ruthenium nanoparticles decorated curl-like porous carbons for high performance supercapacitors. *Sci Rep* 6:19949. <https://doi.org/10.1038/srep19949>
- Okutucu C, Duman G, Ucar S, Yasa I, Yanik J (2011) Production of fungicidal oil and activated carbon from pistachio shell. *J Anal Appl Pyrolysis* 91(1):140–146. <https://doi.org/10.1016/j.jaap.2011.02.002>
- Hassan A, Youssef A, Priece P (2013) Removal of deltamethrin insecticide over highly porous activated carbon prepared from pistachio nutshells. *Carbon Lett* 14(4):234–242. <https://doi.org/10.5714/CL.2013.14.4.234>
- Xu J, Gao Q, Zhang Y, Tan Y, Tian W, Zhu L, Jiang L (2014) Preparing two-dimensional microporous carbon from pistachio nutshell with high areal capacitance as supercapacitor materials. *Sci Rep* 4(5545). <https://doi.org/10.1038/srep05545>

11. Wu F, Tseng R, Hu C, Wang C (2005) Effects of pore structure and electrolyte on the capacitive characteristics of steam-and KOH activated carbons for supercapacitors. *J Power Sources* 144(1):302–309. <https://doi.org/10.1016/j.jpowsour.2004.12.020>
12. Veerakumar P, Veeramani V, Chen SM, Madhu R, Liu SB (2016) Palladium nanoparticle incorporated porous activated carbon: electrochemical detection of toxic metal ions. *ACS Appl Mater Interfaces* 8(2):1319–1326. <https://doi.org/10.1021/acsami.5b10050>
13. Zhang L, Ye C, Li X, Ding Y, Liang H, Zhao G, Wang YA (2018) CuNi/C nanosheet array based on a metal–organic framework derivative as a supersensitive non-enzymatic glucose sensor. *Nano-Micro Lett* 10(1):28. <https://doi.org/10.1007/s40820-017-0178-9>
14. Wu J, Shan S, Luo J, Joseph P, Petkov V, Zhong CJ (2015) PdCu nanoalloy electrocatalysts in oxygen reduction reaction: role of composition and phase state in catalytic synergy. *ACS Appl Mater Interfaces* 7(46):25906–25913. <https://doi.org/10.1021/acsami.5b08478>
15. Xu C, Liu A, Qiu H, Liu Y (2011) Nanoporous PdCu alloy with enhanced electrocatalytic performance. *Electrochem Commun* 13(8):766–769. <https://doi.org/10.1016/j.elecom.2011.04.007>
16. Liu A, Geng H, Xu C, Qiu H (2011) A three-dimensional hierarchical nanoporous PdCu alloy for enhanced electrocatalysis and biosensing. *Anal Chim Acta* 703(2):172–178. <https://doi.org/10.1016/j.aca.2011.07.039>
17. Yang H, Wang Z, Li C, Xu C (2017) Nanoporous PdCu alloy as an excellent electrochemical sensor for H₂O₂ and glucose detection. *J Colloid Interface Sci* 491(1):321–328. <https://doi.org/10.1016/j.jcis.2016.12.041>
18. Mehmeti E, Stanković DM, Chaiyo S, Švorc L, Kalcher K (2016) Manganese dioxide-modified carbon paste electrode for voltammetric determination of riboflavin. *Microchim Acta* 183(5):1619–1624. <https://doi.org/10.1007/s00604-016-1789-4>
19. Sriramprabha R, Divagar M, Ponpandian N, Viswanathan C (2018) Tin oxide/reduced graphene oxide nanocomposite-modified electrode for selective and sensitive detection of riboflavin. *J Electrochem Soc* 165(11):B498–B507. <https://doi.org/10.1149/2.0761811jes>
20. Parvin MH, Azizi E, Arjomandi J, Lee JY (2018) Highly sensitive and selective electrochemical sensor for detection of vitamin B₁₂ using an Au/PPy/FMNP_s@TD-modified electrode. *Sensors Actuators B Chem* 261:335–344. <https://doi.org/10.1016/j.snb.2018.01.168>
21. Roushani M, Shahdost-fard F (2015) A novel ultrasensitive aptasensor based on silver nanoparticles measured via enhanced voltammetric response of electrochemical reduction of riboflavin as redox probe for cocaine detection. *Sensors Actuators B Chem* 207:764–771. <https://doi.org/10.1016/j.snb.2014.10.131>
22. Chen M, Andrenyak DM, Moody DE, Foltz RL (2005) Determination of riboflavin by high-performance liquid chromatography with riboflavin-depleted urine as calibration and control matrix. *J Chromatogr B* 820(1):147–150. <https://doi.org/10.1016/j.jchromb.2005.03.018>
23. Ashraf M, Javed S, Abbas Q, Khokhar MY, Nangyal H, Sherwani SK, Kausar R (2014) Spectrophotometric determination of riboflavin with spermine-copper chloride complexes in pharmaceutical preparations. *Am Euras J Agric Environ Sci* 14:1397–1401. <https://doi.org/10.5829/idosi.aejas.2014.14.12.9189>
24. Shumyantseva VV, Bulko TV, Petushkova NA, Samenkova NF, Kuznetsova GP, Archakov AI (2004) Fluorescent assay for riboflavin binding to cytochrome P450 2B4. *J Inorg Biochem* 98(2):365–370. <https://doi.org/10.1016/j.jinorgbio.2003.10.024>
25. Arnold A, Lipsius ST, Greene DJ (1941) Riboflavin determination by the microbiological method. *J Food Sci* 6(1):39–43. <https://doi.org/10.1111/j.1365-2621.1941.tb16266.x>
26. Muthusankar G, Rajkumar C, Chen SM, Karkuzhali R, Gopu G, Sangili A, Sengottuvelan N, Sankar R (2019) Sonochemical driven simple preparation of nitrogen-doped carbon quantum dots/SnO₂ nanocomposite: a novel electrocatalyst for sensitive voltammetric determination of riboflavin. *Sensors Actuators B* 281(15):602–612. <https://doi.org/10.1016/j.snb.2018.10.145>
27. Kariuki NN, Wang X, Mawdsley JR, Ferrandon MS, Niyogi SG, Vaughney JT, Myers DJ (2010) Colloidal synthesis and characterization of carbon-supported Pd–Cu nanoparticle oxygen reduction electrocatalysts. *Chem Mater* 22(14):4144–4152. <https://doi.org/10.1021/cm100155z>
28. Veerakumar P, Salamalai K, Thanasekaran P, Lin KC (2018) Simple preparation of porous carbon-supported ruthenium: propitious catalytic activity in the reduction of ferrocyanate(III) and a cationic dye. *ACS Omega* 3(10):12609–12621. <https://doi.org/10.1021/acsomega.8b01680>
29. Yang ZR, Wang SQ, Wang J, Zhou AJ, Xu CW (2017) Pd supported on carbon containing nickel, nitrogen and sulfur for ethanol electrooxidation. *Sci Rep* 7:15479. <https://doi.org/10.1038/s41598-017-15060-x>
30. Karnan M, Subramani K, Srividhya PK, Sathish M (2017) Electrochemical studies on comcob derived activated porous carbon for supercapacitors application in aqueous and non-aqueous electrolytes. *Electrochim Acta* 228(20):586–596. <https://doi.org/10.1016/j.electacta.2017.01.095>
31. Kim D, Kim JM, Jeon Y, Lee J, Oh J, Antink WH, Kim D, Piao Y (2018) Novel two-step activation of biomass-derived carbon for highly sensitive electrochemical determination of acetaminophen. *Sensors Actuators B Chem* 259(15):50–58. <https://doi.org/10.1016/j.snb.2017.12.066>
32. Apaydin-Varol E, Putun E, Putun AE (2007) Slow pyrolysis of pistachio shell. *Fuel* 86(12–13):1892–1899. <https://doi.org/10.1016/j.fuel.2006.11.041>
33. Chen D, Sun P, Liu H, Yang J (2017) Bimetallic Cu–Pd alloy multipods and their highly electrocatalytic performance for formic acid oxidation and oxygen reduction. *J Mater Chem A* 5(9):4421–4429. <https://doi.org/10.1039/C6TA10476B>
34. Han SH, Bai J, Liu HM, Zeng JH, Jiang JX, Chen Y, Lee JM (2016) One-pot fabrication of hollow and porous Pd–Cu alloy nanospheres and their remarkably improved catalytic performance for hexavalent chromium reduction. *ACS Appl Mater Interfaces* 8(45):30948–30955. <https://doi.org/10.1021/acsami.6b10343>
35. Laviron E (1974) Adsorption, autoinhibition and autocatalysis in polarography and in linear potential sweep voltammetry. *J Electroanal Chem* 52(3):355–393. [https://doi.org/10.1016/S0022-0728\(74\)80448-1](https://doi.org/10.1016/S0022-0728(74)80448-1)

Publisher's note Springer Nature remains neutral with regard to jurisdictional claims in published maps and institutional affiliations.